Slow-rotation dynamic SPECT with a temporal second derivative constraint

T. Humphries,[1] A. Celler,[2, a)] and M. Trummer[1]

[1)] *Department of Mathematics, Simon Fraser University, Burnaby, British Columbia, Canada, V5A 1S6*

[2)] *Department of Radiology, University of British Columbia, Vancouver, British Columbia, Canada, V5Z 1L8*

(Dated: 12 January 2011)

Purpose: Dynamic tracer behavior in the human body arises as a result of continuous physiological processes. Hence, the change in tracer concentration within a region of interest (ROI) should follow a smooth curve. We propose a modification to an existing slow-rotation dynamic SPECT reconstruction algorithm (dSPECT) with the goal of improving the smoothness of time activity curves (TACs) and other properties of the reconstructed image.

Methods: The new method, denoted d^{2}EM, imposes a constraint on the second derivative (concavity) of the TAC in every voxel of the reconstructed image, allowing it to change sign at most once. Further constraints are enforced to prevent other non-physical behaviors from arising. The new method is compared to dSPECT using digital phantom simulations and experimental dynamic ^{99m}Tc-DTPA renal SPECT data, to assess any improvement in image quality.

Results: In both phantom simulations and healthy volunteer experiments, the d^{2}EM method provides smoother TACs than dEM, with more consistent shapes in regions with dynamic behavior. Magnitudes of TACs within an ROI still vary noticeably in both dSPECT and d^{2}EM images, but also in images produced using an OSEM approach that reconstructs each time frame individually, based on much more complete projection data. TACs produced by averaging over a region are similar using either method, even for small ROIs. Results for experimental renal data show expected behavior in images produced by both methods, with d^{2}EM providing somewhat smoother mean TACs and more consistent TAC shapes.

Conclusion: The d^{2}EM method is successful in improving the smoothness of time activity curves obtained from the reconstruction, as well as improving consistency of TAC shapes within ROIs.

PACS numbers: 87.57.uh, 87.57.nf

Keywords: dynamic SPECT, slow rotation, dSPECT, iterative reconstruction, constrained optimization

[a)]Email: aceller@phas.ubc.ca

I. INTRODUCTION

In single photon emission computed tomography (SPECT), the distribution of a radioactive tracer inside a patient is estimated based on a set of projections acquired sequentially as the camera rotates around him or her. In a conventional SPECT study, the tracer distribution is assumed to be static during acquisition. There are applications, however, where it would be useful to administer an agent with fast uptake and washout, and to assess function by measuring the rate at which the activity concentration changes.

Many dynamic SPECT methods have been developed since the mid-1990s; an excellent review is presented in [1]. One approach is to perform repeated fast (e.g. 5- to 60-second) rotations of the camera to acquire multiple sets of projection data. Projections acquired in a single rotation are then assumed to be consistent, and a series of 3D images (time frames) is reconstructed using a conventional static SPECT algorithm such as ordered subsets expectation maximization (OSEM)[2]. This approach has been studied most notably for ^{99m}Tc-Teboroxime cardiac imaging[3–10], as well as applications such as lung[11] and kidney[12] imaging. Images produced by this method, however, tend to be noisy and suffer from artifacts due to the changing tracer distribution and the low number of counts acquired per projection. Other fast-rotation approaches, therefore, estimate kinetic parameters directly from projection data using kinetic modeling[13–16], to avoid bias due to image artifacts. A modification of this approach improves computational efficiency by using spatiotemporal B-spline basis functions to represent the time activity curve (TAC) in every voxel[17,18]. A third method uses a 4D maximum *a posteriori* (MAP) algorithm with a compartmental model-based prior, which encourages TACs to conform to the model[19].

All of these approaches require a camera capable of multiple fast rotations. Dedicated cardiac camera systems[20,21] which are well-suited to dynamic studies have also been developed in recent years. These cameras use novel geometries and improved detection to increase sensitivity and acquire multiple views through a patient simultaneously, without the use of a rotating camera gantry. Dynamic SPECT reconstruction using these cameras typically follows the same principle as the early fast rotation methods; namely, a conventional technique such as OSEM is used to reconstruct each time frame of the image separately. No temporal consistency between time frames of the dynamic image is enforced using this approach, as each time frame is reconstructed based only on the data corresponding to that frame.

At the present time the vast majority of systems available in clinics are standard SPECT systems which acquire data over a single slow camera rotation (10-20 minutes), precluding the use of these methods. Dynamic SPECT imaging on these systems requires reconstructing an image from extremely inconsistent projection data, as the tracer distribution changes drastically during the acquisition. As a result, one must make assumptions about the dynamic behavior of the tracer in order to obtain a sensible image. Early methods[22,23] assumed that activity decayed exponentially in every voxel, and estimated the decay coefficients directly from the projection data. The factor analysis approach,[24] meanwhile, assumes that the dynamic activity in every voxel is a linear combination of a small number of time-dependent functions (factors). The reconstruction algorithm then determines the shapes of these factors and the coefficient of each factor in every dynamic voxel.

Our dSPECT method[25–27] is another approach which constrains the solution by restricting the temporal behavior of activity in every voxel, using linear inequalities. In particular, activity in a voxel is allowed only to increase, decrease, or increase to a peak value and then decrease. In essence, the first derivative of every TAC is allowed to change sign at most once. The constraint is independently imposed on every voxel, allowing different behavior in different regions of the image if required. This method eliminates a large number of unphysical solutions which still fit the projection data well, and unlike other approaches, does not require any *a priori* determination of a suitable set of basis functions or factors to model the temporal behavior. Although initially developed for single slow rotation dynamic SPECT reconstruction, the main characteristic of the dSPECT method is that it processes all data simultaneously. Thus, it can also be applied in cases where more complete projection data is available – such as dynamic positron emission tomography or dynamic imaging on the new dedicated cardiac systems – to link frames of the image temporally.

Since dynamic tracer behavior within the body arises as a result of continuous physiological processes, we expect that the TACs for a given region of interest (ROI) should be fairly smooth, provided adequate temporal sampling. While dSPECT does eliminate many nonphysical solutions, it does not require the TAC in every voxel to be smooth. As a result, TACs with unphysical behavior, such as sharp spikes, have been observed in images reconstructed with dSPECT. In this paper, we propose a modification to dSPECT which instead of acting on the first derivative, constrains the second derivative of the TAC in every image voxel. The method, denoted d^{2}EM, guarantees smoother TACs than dSPECT. Using digital

phantom simulations and preliminary experiments on a healthy volunteer, we investigate the performance of the new method to assess whether it improves image quality.

II. METHOD

A. dSPECT algorithm

The dSPECT constraint is imposed with a *difference tensor*, denoted A, which acts on the vector x representing the 4D distribution of activity to define a new vector,

$$\tilde{x} = Ax. \tag{1}$$

The tensor maps the vector x, consisting of the activity values in every voxel at every time frame, to the vector $\tilde{x}$, consisting of activity *differences* between sequential time frames for every voxel. The dSPECT algorithm then iteratively optimizes over $\tilde{x}$ using either a constrained least squares (CLS) or dynamic expectation maximization (dEM) approach. In this study we consider only the latter, as it is more computationally efficient[28]. The dEM update formula is analogous to maximum likelihood expectation maximization (MLEM)[29]:

$$\tilde{x}_{i,k}^{(n+1)} = \frac{\tilde{x}_{i,k}^{(n)}}{\sum_j \left(C_{ij,k}A_{i,k}^{-1}\right)} \sum_j C_{ij,k}A_{i,k}^{-1} \frac{p_{j,k}}{\sum_i C_{ij,k}A_{i,k}^{-1}\tilde{x}_{i,k}^{(n)}}, \tag{2}$$

where p is the vector of acquired projection data, C is the system matrix modeling the propagation of photons from the patient body to the detector, i is the index corresponding to voxels in image space, j is the index corresponding to pixels in projection space, and k is the temporal index corresponding to each time frame. In dSPECT, every projection is assumed to correspond to a different distribution of activity, so the total number of time frames reconstructed is equal to the number of camera stops. The system matrix may include standard SPECT effects such as depth-dependent collimator response and patient-specific attenuation. Attenuation correction is particularly important in slow-rotation dynamic SPECT, since without it one cannot separate the effect of attenuation on the projection data, which varies as the camera rotates, from the effect of changing tracer distribution.

The fact that the dEM update formula (2) preserves positivity of $\tilde{x}$ allows the desired temporal behavior to be imposed on every voxel by A. For instance, to impose strictly increasing behavior on voxel i, $\tilde{x}$ contains the entries $(x_{i,2} - x_{i,1})$, $(x_{i,3} - x_{i,2})$, etc. Since

these differences are positive in $\tilde{x}$, mapping $\tilde{x}$ back to x results in an increasing TAC. For increasing behavior, $\tilde{x}$ also contains $x_{i,1}$, the activity value in the first time frame. This provides a one-to-one mapping between x and $\tilde{x}$, and ensures that the TAC for voxel i remains positive. Decreasing behavior is enforced similarly. For a TAC that increases and then decreases, the time of peak activity is not known *a priori*, so the algorithm allows the assumed time-to-peak for every voxel to be adjusted in between iterations, based on the data. Then increasing behavior can be enforced prior to the peak point, and decreasing behavior afterwards.

B. Second derivative constraint

In this paper we introduce a dEM-like algorithm, denoted by d^{2}EM, that imposes a second derivative (concavity) constraint on the TAC in every voxel. Just as dEM allows the first derivative of the TAC in every voxel to change sign at most once, d^{2}EM allows the concavity of the TAC to change at most once; from concave up to concave down, or vice-versa. The first derivative may only change sign once as well, to ensure that any solution generated by d^{2}EM satisfies the dSPECT first-derivative constraint. The constraint is imposed in the same way as in dEM, using a modified difference tensor and the fact that the update formula (2) preserves positivity of the vector $\tilde{x}$. In d^{2}EM, rather than consisting of activity differences, $\tilde{x}$ consists mostly of second differences. For instance, the mapping

$$\tilde{x}_{i,k} = x_{i,k-1} - 2x_{i,k} + x_{i,k+1} \tag{3}$$

forces the right-hand side to be positive, ensuring that the TAC for voxel i has a positive second derivative (concave up) at time frame k. Some first difference and activity values at the endpoints of the TAC are also included in $\tilde{x}$, to ensure positivity of the TAC and maintain a one-to-one mapping with x.

Since the shape of the TAC in every voxel is not known *a priori*, the d^{2}EM algorithm must allow the assumed behavior to be adjusted in between iterations, based on the data. As mentioned earlier, in dEM the assumed time of peak activity in a voxel can shift to an earlier or later time frame, if the data suggest that the current assumption is incorrect. Since d^{2}EM is based on the second derivative, it is the time of the inflection point, where the concavity of the TAC changes, that is adjusted. So, for instance, if the TAC in a voxel

is initially assumed to be entirely concave down, but the data suggest that the latter part of the TAC should be concave up, then this part of the TAC will approach zero concavity after several iterations of the algorithm. This situation indicates that the assumed behavior for that voxel should instead be a TAC that is initially concave down, then concave up.

III. EXPERIMENTS

A. Annulus phantom simulation

The performance of d^{2}EM was first tested using two simple 64x64-voxel annulus phantoms, denoted A and B, which were similar to those used in some previous studies[27,30,31]. The annulus in both phantoms was subdivided into four regions of equal size, and surrounded by low-intensity, constant background activity. Additionally, a circular "cold" region containing no activity was included inside the annulus. Dynamic activity for each region was generated over 64 time frames, using a dual-exponential function:

$$x(t) = A_0 \left(-e^{-\lambda_1 t} + e^{\lambda_2 t} \right), \tag{4}$$

where λ_1 and λ_2 were varied in each region to model different behavior. The phantoms and the associated TACs are illustrated in Fig. 1. In order to assess the performance of the method for a variety of dynamic situations, Phantom A featured relatively fast uptake and washout of activity (half-life of 2 to 16 minutes), while in Phantom B the washout was more gradual (20 minutes).

Acquisition was modeled as a dual-head (90° mode) full rotation (360° per head) over 20 minutes, with 64 stops (roughly 20 seconds per frame). Projections were generated analytically, with Poisson noise added afterwards in proportion to the total counts. No attenuation or collimator blurring were included in the projection model. Images were reconstructed using 60 iterations of both dEM and d^{2}EM, as further iterations did not noticeably improve image quality.

To provide further context, dynamic images of the two phantoms were also reconstructed using an OSEM-based approach. For these images, projection data consisting of 64 views around the object for *each* of the 64 time frames was generated, modeling a ring SPECT-like system with 64 heads. Thus, 32 times as many views were acquired per time frame (compared to the projection data used by dEM and d^{2}EM), while the counts for each view

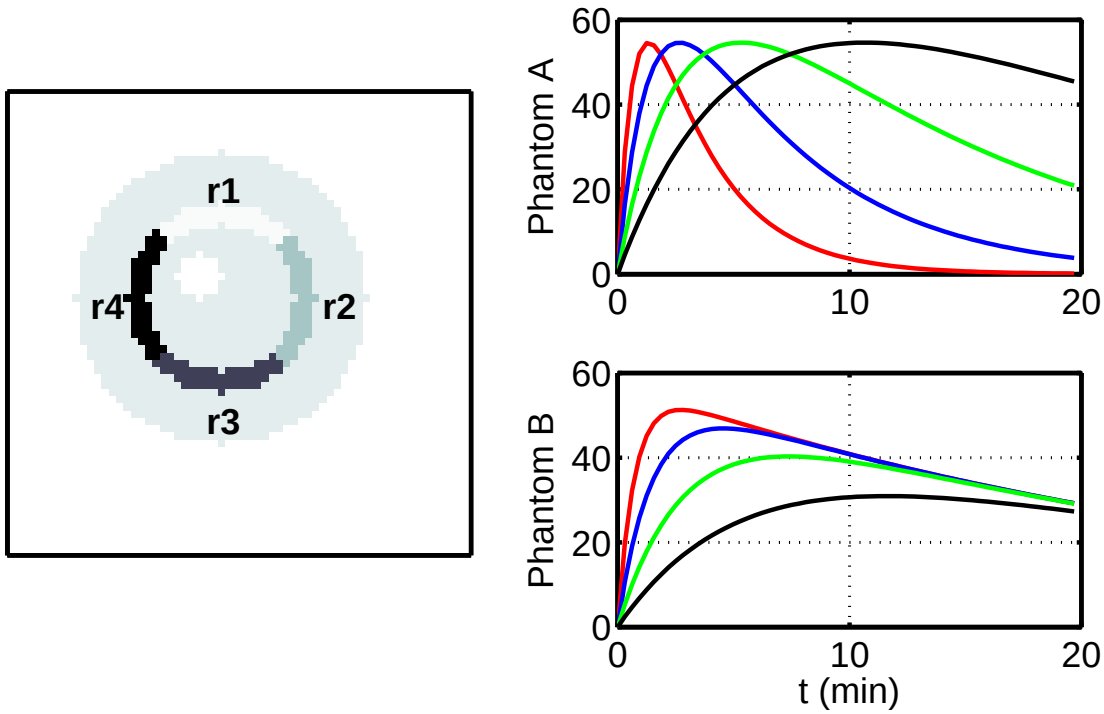

FIG. 1. Annulus phantom used for computer simulation. Left: Image of a single time frame of the phantom, showing the four regions plus cold spot. Right: TACs for each of the four regions in Phantom A (top) and Phantom B (bottom), showing the number of counts in each voxel as a function of time. Red, blue, green and black TACs correspond to regions 1, 2, 3 and 4, respectively. Background activity was 5 counts/voxel.

were not reduced, as they would be by a fast-rotating camera. Six iterations of OSEM with 8 subsets were then used to reconstruct each frame of the dynamic images separately. These images provided a "gold standard" against which to judge the performance of the two other methods.

For analysis of the results, ROIs were defined for each of the four annulus regions, using the true boundaries. The images were then compared using the following measures:

1. The mean TAC was computed for each ROI and then compared to the true one. The relative error of the mean TAC was calculated as

$$\varepsilon = \left\| \tau^{\mathrm{rec}} - \tau^{\mathrm{tr}} \right\|_2 \Big/ \left\| \tau^{\mathrm{tr}} \right\|_2 \times 100\% \tag{5}$$

where $\|\cdot\|_2$ is the l^2 norm (Euclidean distance), τ^{rec} is the 1×64 vector representing the mean TAC for that region obtained from the reconstructed image, and τ^{tr} the equivalent vector representing the true TAC. This error provided a measure of how well each method performed in an aggregate sense over the entire ROI.

2. Weighted relative standard deviation between TACs in every voxel of the ROI was calculated as

$$\bar{\sigma} = \sum_{k=1}^{K} W_k \frac{\sigma_k}{\nu_k} \times 100\%, \tag{6}$$

where σ_k is the standard deviation between true and reconstructed activities at time k for every voxel in the ROI, ν_k is the true activity at time k for a voxel in the ROI, and the weighting factor is

$$W_k = \nu_k \Big/ \sum_{k'=1}^{K} \nu_{k'}.$$

This was a more severe error measure than ε, as it penalized deviation from the true TAC in any voxel, rather than comparing an aggregate TAC over the whole region. It quantified the amount of variation that occurred within a region of the reconstructed image that was known to be spatially uniform in truth.

3. An average relative "shape error" was calculated for each region of interest using the following formula:

$$\mathcal{S} = \frac{1}{I} \sum_{i=1}^{I} \left(\left\| \tau^{\mathrm{tr}} - \alpha_i \tau_i^{\mathrm{rec}} \right\|_2 \Big/ \left\| \tau^{\mathrm{tr}} \right\|_2 \right) \times 100\% \tag{7}$$

where I is the number of voxels in the ROI, τ_i^{rec} is the 1×64 vector representing the reconstructed TAC in voxel i, τ^{tr} is the true TAC vector for that ROI, and α_i is the scaling factor which minimizes the l^2 norm difference between the two vectors:

$$\alpha_i = \frac{\tau^{\mathrm{tr}} \cdot \tau_i^{\mathrm{rec}}}{\tau_i^{\mathrm{rec}} \cdot \tau_i^{\mathrm{rec}}}.$$

(Here $\cdot$ is the dot product between the two vectors). The average shape error was used to measure how consistent the shapes of TACs were inside each ROI, while ignoring their magnitudes. If the shape of the TAC in a voxel of the reconstructed image was close to the true shape, then the difference between them would be small after scaling; if their shapes were different, then the difference would still be relatively large. A small value of $\mathcal{S}$ meant that the kinetic behavior indicated by the TACs at the voxel level was generally correct, even if there was variation in magnitude.

4. The time-to-peak activity was recorded for every voxel in each ROI, and the mean and standard deviation of times-to-peak were calculated. This measure was intended to assess how consistent the time-to-peak in every voxel was in each region, as time-to-peak is often a quantity of interest in dynamic imaging.

The TACs in the "cold" region were also examined, but these error measures were not calculated since they are not applicable to a region with no activity.

B. Healthy volunteer experiment

One potential clinical application of dynamic SPECT is assessment of renal function by examining washout of ^{99m}Tc-DTPA or ^{99m}Tc-MAG3 in the kidneys. Current clinical protocol for dynamic renal imaging typically consists of a planar scintigram acquired from behind the patient. By drawing 2D ROIs over the cortex region of each kidney, it is possible to obtain a TAC for each kidney as a qualitative measure of renal function. Planar imaging, however, is unable to correct for patient-specific attenuation and effects due to organ overlap; both of which are accounted for in a 3D SPECT scan.

Dynamic ^{99m}Tc-DTPA (370 MBq) renal images of a single consenting healthy adult volunteer were acquired using a dual-head Siemens Symbia T2 SPECT/CT system with detectors positioned at 90°, and attenuation correction data provided by the 2 slice CT scanner. The camera rotated over 360° per head, with 64 stops lasting 20 seconds each. Images consisting of forty-four 128×128-voxel slices and sixty-four 20 second time frames were reconstructed using 80 iterations of both dEM and d^{2}EM. Voxels were 4.79 mm per side, and the effects of attenuation and collimator blurring were incorporated into the system matrix. As mentioned in Section II, attenuation correction is essential to separate the effects of attenuation on projection data from those of tracer kinetics. In the absence of a SPECT/CT system, an attenuation map from a transmission scan or separately acquired CT image would be necessary.

Since the true distribution of activity was not known in this experiment, it was not possible to use the same quality measures as in the phantom simulations. Nor was it possible to compute OSEM-based images as a point of comparison, since no equipment capable of acquiring multiple views of the patient simultaneously was available. Additionally, while activity distributions in the phantom simulations were known to be spatially uniform within ROIs, in reality each living kidney may contain several regions with different dynamic behaviors. In particular, uptake in the renal pelvis occurs later than in the cortex since DTPA filters through the cortex before arriving at the pelvis; furthermore, the cortex itself is comprised of numerous individual lobes, which may also exhibit different concentrations of

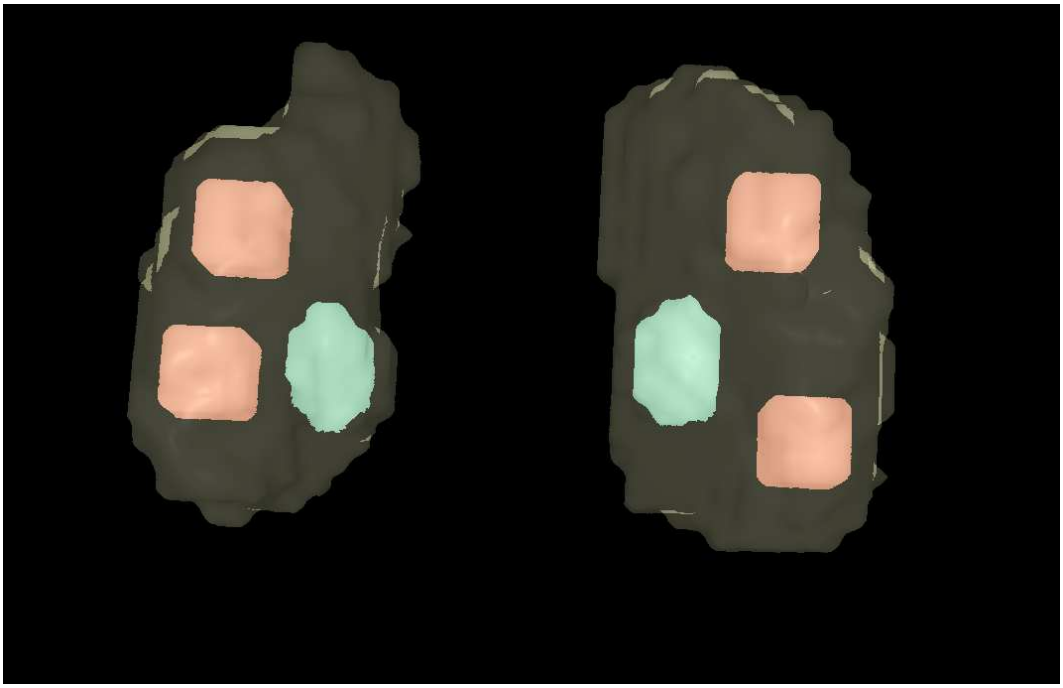

FIG. 2. Volume rendering of segmentation used for healthy volunteer renal data (posterior view). Faint outline shows left and right kidney cortices, with pelves shown in blue and ROIs shown as red cubes. Light patches around edges appear due to the volume rendering. *Figure prepared with the assistance of A. Saad.*[33]

activity or time-to-peak[32]. Thus, assuming uniform dynamic behavior in an entire kidney could lead to misleading evaluations.

Thus, in order to analyze the reconstructed images, small ROIs were defined in the cortex regions of each kidney. To generate these ROIs, the image was first segmented into four regions corresponding to the left and right kidney cortices and pelves, using a user-assisted dynamic segmentation algorithm[33]. By examining the segmentation, $4 \times 4 \times 4$-voxel cubes, corresponding to a real volume of about 7 cm^3, were then defined in the inferior and superior regions of each kidney, giving four ROIs in total (Fig. 2). Due to the small size of each ROI, the true behavior within them was expected to be fairly consistent. Weighted relative standard deviation and average shape error were calculated for each region, with the mean TAC for the region used as a surrogate for the true TAC in formulas (6) and (7). Mean and standard deviation of time-to-peak within each ROI were also calculated.

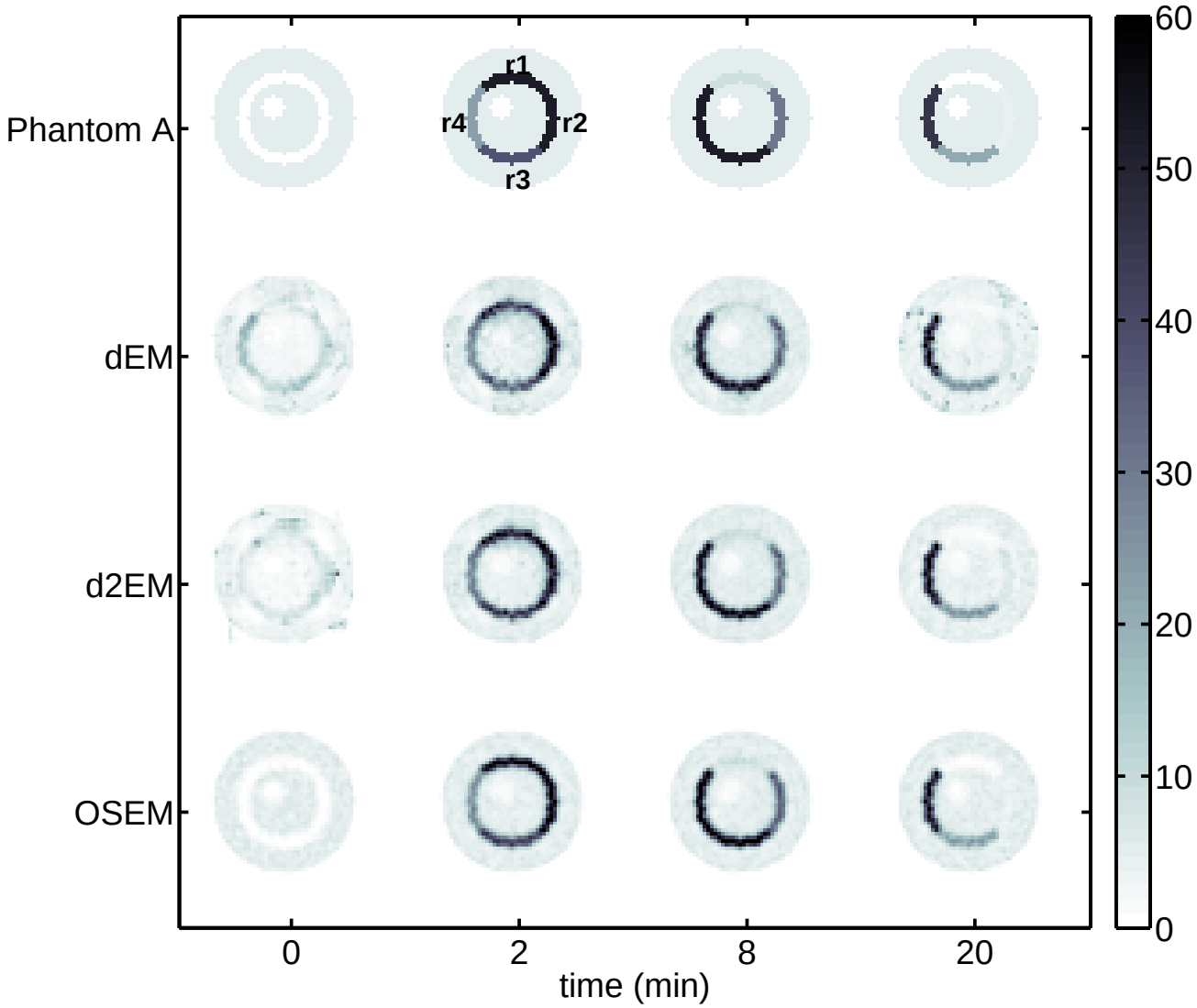

FIG. 3. Selected 64x64-voxel time frames of reconstructed annulus phantom images, for Phantom A. Top row shows frames from the phantom (the truth), second row the corresponding frames from the dEM image, third row the d^{2}EM image, and fourth row the frame-by-frame OSEM image.

IV. RESULTS

Time frames of the true phantom and of the three reconstructed images for Phantom A are shown in Fig. 3. Images of Phantom B are not shown, but were qualitatively similar. Fig. 4 shows individual voxel TACs from each ROI of the dEM, d^{2}EM and frame-by-frame OSEM images for both phantoms, as well as the true and mean TACs for the ROI. The calculated error measures, ε, $\bar{\sigma}$, $\mathcal{S}$, and mean $\pm$ standard deviation of time-to-peak, are shown in Table I.

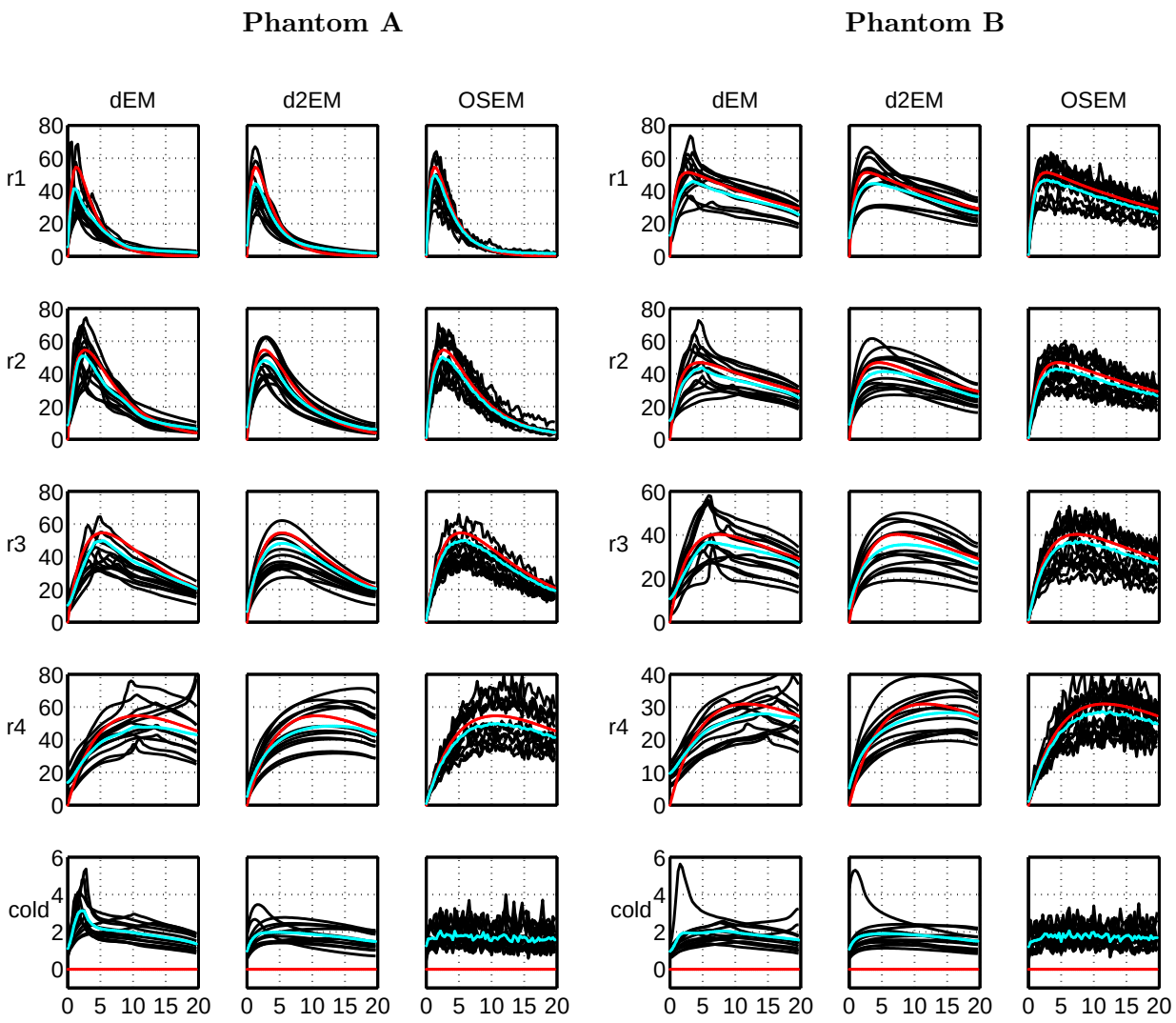

FIG. 4. Representative voxel TACs (counts vs time) from each ROI for the two annulus phantoms, from images reconstructed using the dEM, d^{2}EM and frame-by-frame OSEM approaches. Voxel TACs shown as black solid lines, with true TAC shown as a red line and mean TAC for the entire region shown as a light blue line. For the purpose of clarity, only the TACs from 12 randomly selected voxels (out of 53 total) in each of the four dynamic regions are shown in each plot. Please note the change in y-axis scale for some regions.

For the healthy volunteer experiment, the mean TAC and voxel TACs for each of the four ROIs are shown in Fig. 5. Error measures are provided in Table II.

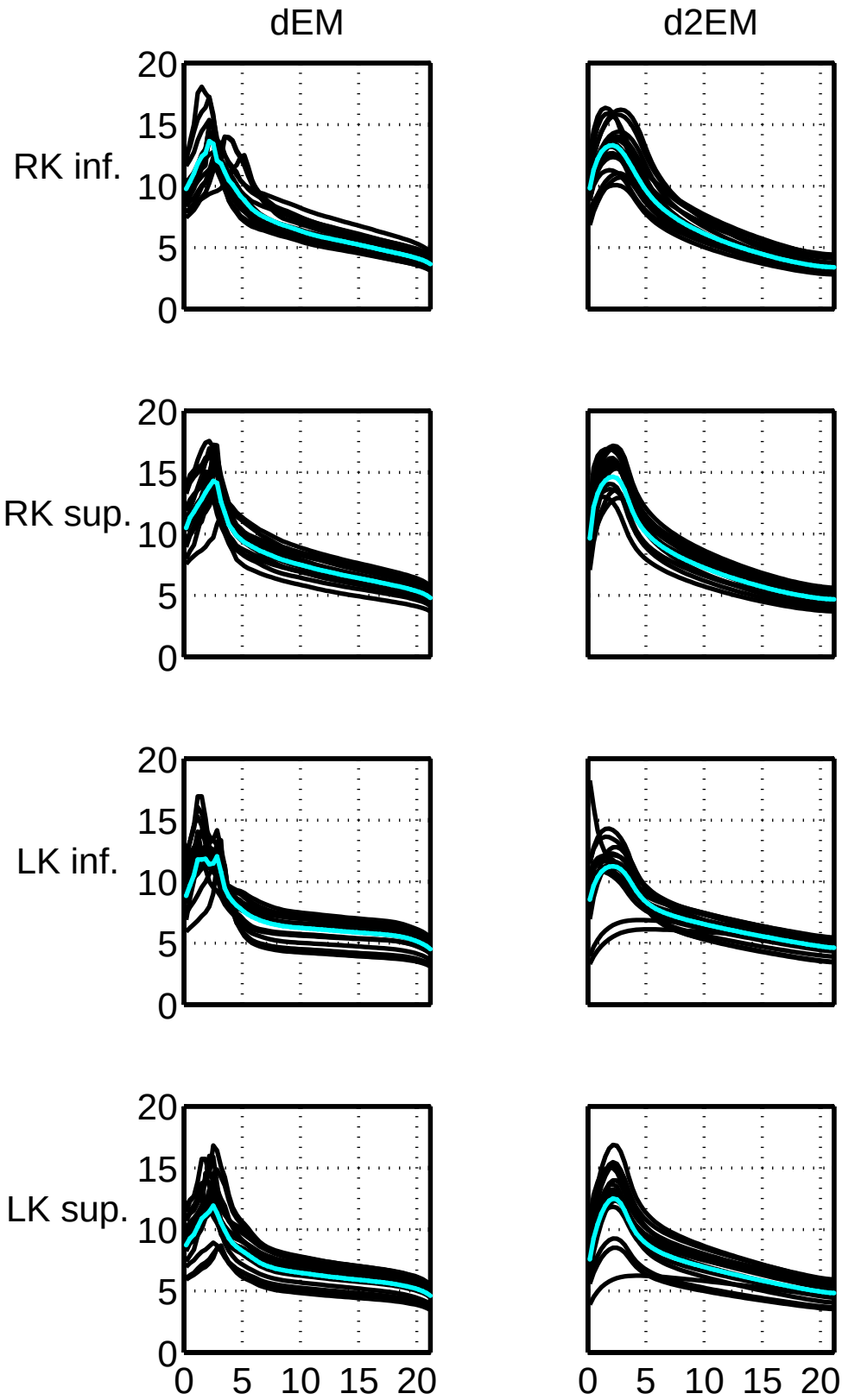

FIG. 5. TACs in the four ROIs (inferior and superior regions of right and left kidneys) in the dynamic renal study, for the dEM (left column) and d^{2}EM (right column) reconstructions. Sixteen randomly selected voxel TACs (out of 64 total) in the region are shown as black solid lines, with the mean TAC for the entire region shown as a light blue line. X-axis shows time in minutes; y-axis shows counts.

Region	Method	Phantom A					Phantom B				
		ε (%)	$\bar{\sigma}$ (%)	$\mathcal{S}$ (%)	true peak (min)	mean peak (min)	ε (%)	$\bar{\sigma}$ (%)	$\mathcal{S}$ (%)	true peak (min)	mean peak (min)
r1	dEM	27.4	45.8	23.6		1.7 ± 0.6	12.7	22.7	10.2		4.4 ± 1.8
	d^{2}EM	20.0	40.8	17.0	1.6	1.8 ± 0.4	11.2	23.0	10.1	3.1	4.9 ± 1.6
	OSEM	9.9	31.9	11.2		1.7 ± 0.3	8.9	22.3	7.1		4.0 ± 1.3
r2	dEM	13.5	25.7	15.2		2.7 ± 0.7	11.2	23.3	10.0		5.6 ± 2.2
	d^{2}EM	13.1	24.0	10.7	3.1	3.1 ± 0.4	10.2	22.8	7.7	5.0	6.0 ± 1.0
	OSEM	8.9	22.5	9.0		3.0 ± 0.6	8.6	22.0	7.1		5.5 ± 1.3
r3	dEM	14.2	24.1	11.1		5.4 ± 1.1	11.2	25.3	11.0		9.3 ± 3.6
	d^{2}EM	10.6	23.4	7.2	5.6	5.9 ± 0.6	10.1	24.0	6.6	7.8	9.1 ± 1.2
	OSEM	9.1	22.6	7.4		5.9 ± 1.0	8.7	22.1	7.4		8.2 ± 1.3
r4	dEM	13.4	26.0	11.3		13.1 ± 3.8	12.8	24.5	12.1		15.2 ± 3.6
	d^{2}EM	10.7	24.5	6.9	10.9	13.4 ± 1.9	10.3	23.6	9.0	11.9	15.4 ± 1.9
	OSEM	9.0	23.7	7.0		11.2 ± 2.2	8.5	21.6	8.8		12.6 ± 2.4

TABLE I. Error measures for dynamic regions in the two annulus simulations. Formulas for ε, $\bar{\sigma}$ and $\mathcal{S}$ are given in equations (5), (6) and (7), respectively. Mean peak shows the average time-to-peak for every TAC in the region, ± the standard deviation among times-to-peak.

V. DISCUSSION

A. Annulus phantom simulation

Most time frames of the reconstructed images (Fig. 3) are fairly similar in appearance whether using dEM or d^{2}EM. The most noticeable differences occur in the first and last time frames. For both Phantoms A and B (the latter is not shown), the last time frame is less noisy using d^{2}EM than dEM, likely due to the stronger d^{2}EM constraint. In the dEM reconstruction, the activity in a given voxel for the final time frame is constrained only by the activity in the same voxel in the second-last time frame; for instance, for increasing activity, the activity in that voxel must be greater in the final frame than in the one before. In d^{2}EM, the activity in the last frame is restricted by the activity in both the second- and

Region	Method	$\bar{\sigma}$ (%)	$\mathcal{S}$ (%)	mean peak (min)
RK inf.	dEM	15.6	7.4	2.7 ± 0.8
	d^{2}EM	15.4	5.2	2.3 ± 0.4
RK sup.	dEM	14.2	6.4	2.6 ± 0.6
	d^{2}EM	13.7	4.4	2.2 ± 0.5
LK inf.	dEM	15.5	11.9	2.4 ± 0.8
	d^{2}EM	14.5	8.4	2.4 ± 0.9
LK sup.	dEM	16.1	5.7	2.5 ± 0.5
	d^{2}EM	16.7	4.0	2.4 ± 0.3

TABLE II. Error measures for regions in the inferior and superior regions of the right and left kidneys in the volunteer patient images.

third-last time frames, since the constraint acts on the concavity of the TAC. Thus, the activity in the final frame is more strongly tied to activity in the preceding frames, and as a result, less variation occurs. The same argument holds for the first time frame. For this phantom, however, the first time frame appears noisy using either method; probably due to the fact that counts in this frame are low.

The time frames reconstructed using frame-by-frame OSEM are visually superior to those obtained using dEM and d^{2}EM, which is to be expected given the greater number of views that were used. The first frame in particular is much more accurately reconstructed. At two minutes (second column of Fig. 3), some blurring is visible around region 1 in the dEM and d^{2}EM images, which is not present in the OSEM image. This artifact is also due to the fact that the dEM and d^{2}EM images are based on data where only two views of the object per time frame are available. Both dEM and d^{2}EM link the time frames of the image together through the temporal constraint, so each reconstructed time frame of the image is affected by views corresponding to preceding and subsequent time frames as well. When the tracer concentration is changing quickly in a region, however, then the projection data corresponding to that region is very inconsistent. As a result, only the views from a small number of angles affect the reconstruction of the region over that time period, and blurring results. In general, however, the dEM and d^{2}EM images are in very good agreement with

the frame-by-frame OSEM image, especially given the much smaller amount of data that was used to reconstruct them.

Analysis of TACs within each region (Fig. 4) reveals more differences. The TACs at the voxel level (black lines) in the d^{2}EM image have more consistent shapes and fewer "outlying" TACs with noticeably different shapes from the true one. In region 4 of Phantom A, for instance, there are several TACs with incorrect dynamic behavior in the dEM image, including some showing increasing uptake rate in the last few time frames, and several with sharp peaks around the 10-minute mark. In the d^{2}EM image, most of the voxel TACs in this region have a very similar shape, although there is still variation in magnitude. This is true in other regions shown in Fig. 4 as well, particularly those with slower washout rates. The voxel TACs in regions 1 and 2 of Phantom A, which have the fastest kinetics, appear similar using either dEM or d^{2}EM.

The voxel TACs obtained from the frame-by-frame OSEM images generally have the correct shape, but are not smooth since each frame has been reconstructed separately, without any constraint or condition on the temporal behavior of the activity in each voxel. The variation in magnitude among voxel TACS within regions appears comparable to that observed in the dEM and d^{2}EM images. Thus, it appears that this spread among voxel TACs is inherent to the reconstruction problem itself – perhaps due the use of an EM-based approach – rather than being a drawback of the dEM and d^{2}EM methods specifically.

The mean TAC in most regions (blue lines) is very similar using either dEM or d^{2}EM, despite the large differences between TAC shapes at the voxel level observable in Fig. 4. Even when each region was subdivided into small contiguous subregions of only 12-15 voxels each, the mean TACs for each subregion were very similar. Thus, the performances of dEM and d^{2}EM are comparable when TACs are averaged over a region, and it is mainly at the voxel level that improvements are apparent. The mean TAC obtained from the frame-by-frame OSEM approach, meanwhile, is somewhat closer to the true TAC (red lines) than the mean TAC obtained using the other two methods; most notably in region 1 of Phantom A, where both dEM and d^{2}EM underestimate the true activity. This underestimation is due to the blurring of this region visible in Fig. 3.

The calculated error measures are summarized in Table I. In general the values of ε using d^{2}EM are somewhat smaller than for dEM, but the improvement is not large since this quantity reflects the error in the mean TAC, which is fairly similar using either method.

Values of $\bar{\sigma}$ also show only an incremental improvement using d^{2}EM, since the variation in TAC magnitudes at the voxel level is comparable, as observed in Fig. 4. Values of $\bar{\sigma}$ obtained from the frame-by-frame OSEM reconstruction are also of roughly the same magnitude in most regions.

The shape error, $\mathcal{S}$, is notably smaller for the d^{2}EM images. This is indicative of the fact that the shapes of TACs in individual voxels were generally more consistent and closer to the true shape when d^{2}EM was used. In some regions, the shape error using d^{2}EM is smaller than that obtained using frame-by-frame OSEM as well; this is probably due to the lack of smoothness among voxel TACs in the frame-by-frame image. The deviation in time-to-peak for ROIs in the d^{2}EM images, meanwhile, is often less than half that of the corresponding region in the dEM image. Deviations are also generally larger for regions with slower washout (Phantom B, region 4 of Phantom A), using either method. This is due to the fact that the activity in these regions does not peak as sharply as in the others, leaving more room for ambiguity about the time of peak activity. Correspondingly, these are the regions that appear to be most improved in the d^{2}EM image in Fig. 4. Using frame-by-frame OSEM, the mean time-to-peak is generally closer to the true peak, but there is still considerable variation in time-to-peak between voxels, especially in regions with slow washout.

A paired t-test on the error measures in all 8 regions considered (both phantoms) indicated that ε, $\bar{\sigma}$ and $\mathcal{S}$ values were all significantly smaller using d^{2}EM over dEM ($p = 0.008$, 0.018 and 0.0004, respectively). Both $\mathcal{S}$ and ε were also considered to be significantly improved ($p < 0.05$) if the two phantoms were considered separately (2 tests with 4 samples). A t-test of the error measures in the d^{2}EM image versus the OSEM image indicated that only ε was significantly smaller in the OSEM images of both phantoms. Thus, d^{2}EM performed comparably to frame-by-frame OSEM in terms of the accuracy of TAC shapes ($\mathcal{S}$) and the amount of variation between TACs ($\bar{\sigma}$), despite the much smaller amount of data used to reconstruct the image.

B. Healthy volunteer experiment

Fig. 5 shows the mean TAC and a sample of voxel TACs for the four cubical ROIs defined in the volunteer study. It is apparent that d^{2}EM has indeed resulted in smoother TACs,

both at the voxel level and on the aggregate. In the inferior left kidney ROI, for instance, the variation in TACs in the dEM image has resulted in a mean TAC that peaks twice, which is most likely unphysical. The mean TAC in the d^{2}EM reconstructed image appears more reasonable, although some voxel TACs do show incorrect behavior, such as strictly decreasing or nearly constant activity. In the other three regions, the peak locations and magnitudes are fairly consistent between the dEM and d^{2}EM images; the main difference is that the TAC in the d^{2}EM image peaks more gradually than in the dEM image. In all cases, peak activity occurs between 2 and 3 minutes on average, which is consistent with the expected renal time-to-peak for DTPA in a healthy adult[32]. Given that abnormal behavior may manifest itself in only a small part of the organ, it is encouraging that both dEM and d^{2}EM provide realistic TACs even for small ROIs such as the ones used here.

The calculated error measures are summarized in Table II. Paired t-testing indicates that $\bar{\sigma}$ was not significantly improved in the dEM image ($p = 0.23$), but the shape error $\mathcal{S}$ was significantly improved ($p = 0.004$). This indicates that the shapes of voxel TACs in the four regions were generally more consistent in the d^{2}EM image, but that there was considerable spread in TAC magnitude using either method. More consistent TAC shapes within an ROI is an improvement since it gives more confidence that averaging the TAC over that ROI (as would most likely be done in a clinical study) gives a good indication of the kinetics in that region; if TAC shapes vary drastically within a region, it is not clear whether the average TAC is physically meaningful. Finally, standard deviation of time-to-peak was not significantly improved, which is not surprising since the washout of tracer in this situation was relatively fast, resulting in a well-defined peak in activity. Overall, the results of the volunteer experiment are consistent with the annulus simulations, despite the much greater complexity of the former. The d^{2}EM algorithm has resulted in smoother TACs and significantly more consistent TAC shapes within each region of interest.

VI. CONCLUSION

In this paper we have presented a novel dynamic SPECT reconstruction algorithm, denoted d^{2}EM, for reconstruction of images from data acquired using a single slow camera rotation. The d^{2}EM method is an extension of the existing dEM algorithm, which provides temporal regularization of the reconstructed image by constraining the first derivative of the

TAC in every image voxel. The d^{2}EM algorithm instead constrains the second derivative of every TAC, allowing it to change sign at most once. The goal of this modification is to provide TACs with smoother shapes than those obtained using dEM, since physiology suggests that uptake and washout of tracers should follow a smooth curve.

Digital phantom experiments indicate that the d^{2}EM algorithm provides some improvements in addition to the smoother temporal behavior that results from the stronger constraint. Voxel TACs in the d^{2}EM images have substantially more consistent shapes within regions of interest, especially when tracer kinetics are relatively slow. Standard deviation of time-to-peak in each voxel in some ROIs of this type has been reduced by a factor of two or more using d^{2}EM (cf. Table I). When averaged over a ROI, the mean TACs provided by either method are quite similar.

An overall measure of the standard deviation between all TACs within a ROI is only incrementally reduced using d^{2}EM. This is indicative of the fact that even though TAC shapes are more consistent, there is still considerable variation in the magnitude of TACs within a ROI using either method. The variation in TAC magnitudes is comparable to that observed when a frame-by-frame OSEM reconstruction approach is used, however, indicating that it does not arise as a result of the dEM/d^{2}EM method. Variation in the magnitude of TACs could potentially be reduced by including some spatial regularization, such as a smoothing prior, into the algorithm.

Dynamic renal ^{99m}Tc-DTPA data were acquired for one healthy adult volunteer. Reconstructed images obtained using both the dEM and d^{2}EM algorithms provided physiologically realistic TACs in four small ROIs defined in the kidneys. TACs obtained from the d^{2}EM reconstruction were noticeably smoother than those obtained from dEM, and had more consistent shapes within each ROI. For renal applications, where uptake and washout take place over several minutes, the smoother TACs provided by d^{2}EM are more in line with the expected physiological behavior. For clinical applications where tracer kinetics are expected to be faster than renal studies (e.g. dynamic cardiac imaging with ^{99m}Tc-Teboroxime), it is not clear whether d^{2}EM would provide better results than dEM, as higher temporal sampling may be needed to expect a smooth TAC. The ability of d^{2}EM to recover accurate, three-dimensional information about dynamic *in vivo* processes could be further validated by comparing dynamic SPECT images reconstructed using d^{2}EM to images of the same dynamic processes using more well-established methods, such as dynamic PET imaging.

Overall, we conclude that the d^{2}EM algorithm provides an improvement on dEM in terms of providing smoother, more consistent TAC shapes within dynamic regions of interest. Additionally, phantom experiments indicate that d^{2}EM performs comparably in many respects to a frame-by-frame OSEM approach, even when much more limited projection data is available to the former. Thus, even in cases where multiple views through the object are available for every frame, d^{2}EM may provide improvements over a separate frame-by-frame reconstruction approach.

ACKNOWLEDGMENTS

We thank Dr. Troy Farncombe for providing the dEM software, as well as for his advice and consultation. We thank the personnel at St. Paul's Hospital, Vancouver, British Columbia, for their assistance in acquiring the volunteer patient data, particularly Dr. Rajpaul Attariwala, Dr. George Sexsmith and Nazma Tarmohamed. Patient data were acquired following approval from the Clinical Research Ethics Board of the University of British Columbia. We thank Ahmed Saad for use of the segmentation software used on the clinical data, and Dr. Joe Qranfal for use of the annulus phantom. The authors acknowledge support from the Natural Sciences and Engineering Research Council of Canada.

REFERENCES

[1]G. T. Gullberg, B. W. Reutter, A. Sitek, J. S. Maltz, and T. F. Budinger, *Phys. Med. Biol.* **55**, p. R111–R191 (2010).

[2]H. Hudson, and R. Larkin, *IEEE Trans. Med. Imag.* **13**, 601–609 (1994).

[3]K. Nakajima, J. Taki, H. Bunko, M. Matsudaira, A. Muramori, I. Matsunari, K. Hisada, and T. Ichihara, *J. Nucl. Med.* **32**, 1273–1277 (1991).

[4]A. Smith, G. Gullberg, P. Christian, and F. Datz, *J. Nucl. Med.* **35**, 484–495 (1994).

[5]A. Smith, and G. Gullberg, *IEEE Trans. Nucl. Sci.* **41**, 1626–1633 (1994).

[6]P.-C. Chiao, E. Ficaro, F. Dayanikli, W. Rogers, and M. Schwaiger, *J. Nucl. Med.* **35**, 1265–1273 (1994).

[7]A. Welch, A. M. Smith, and G. T. Gullberg, *Medical Physics* **22**, 1829–1836 (1995), URL `http://link.aip.org/link/?MPH/22/1829/1`.

[8]A. M. Smith, G. T. Gullberg, and P. E. Christian, *J. Nucl. Cardiol.* **3**, 130–142 (1996).

[9]S. G. Ross, A. Welch, G. T. Gullberg, and R. H. Huesman, *Phys. Med. Biol.* **42**, 2193–2213 (1997).

[10]D. J. Kadrmas, E. V. DiBella, R. H. Huesman, and G. T. Gullberg, *Phys. Med. Biol.* **44**, 1997–2014 (1999).

[11]K. Suga, K. Nishigauchi, N. Kume, S. Koike, K. Takano, O. Tokuda, T. Matsumoto, and N. Matsunaga, *J. Nucl. Med.* **37**, 807–814 (1996).

[12]C. Miyazaki, H. Harada, N. Shuke, A. Okizaki, M. Miura, and T. Hirano, *Ann. Nucl. Med* **24**, 189–195 (2010).

[13]G. Zeng, G. Gullberg, and R. Huesman, *IEEE Trans. Nucl. Sci.* **42**, 2339–2346 (1995).

[14]B. Reutter, G. Gullberg, and R. Huesman, *Nuclear Science, IEEE Transactions on* **45**, 3007–3013 (1998), ISSN 0018-9499.

[15]B. Reutter, G. Gullberg, and R. Huesman, "Kinetic parameter estimation from dynamic cardiac patient SPECT projection measurements," in *Nuclear Science Symposium Conference Record, 1998 IEEE*, 1998, pp. 1953–1958.

[16]R. Huesman, B. Reutter, G. Zeng, and G. Gullberg, *Phys. Med. Biol.* **43**, 973–982 (1998).

[17]B. Reutter, G. Gullberg, and R. Huesman, *IEEE Trans Med. Imag.* **19**, 434–450 (2000).

[18]B. Reutter, G. Gullberg, and R. Huesman, *Phys. Med. Biol.* **47**, 2673–2683 (2002).

[19]D. J. Kadrmas, and G. Gullberg, *Phys. Med. Biol.* **46**, 1553–1574 (2001).

[20]S. Gambhir, D. Berman, J. Ziffer, M. Nagler, M. Sandler, J. Patton, B. Hutton, T. Sharir, Sh. Ben Haim, and Si. Ben Haim, *J. Nucl. Med.* **50**, 635–643 (2009).

[21]P. Slomka, D. Berman, and G. Germano, *Current Cardiovascular Imaging Reports* **3**, 162–170 (2010).

[22]M.A. Limber, M.N. Limber, A. Celler, J. Barney, and J. Borwein, *IEEE Trans. Nucl. Sci.* **42**, 1249–1256 (1995).

[23]E. Haber, D. Oldenburg, T. Farncombe, and A. Celler, *IEEE Trans. Nucl. Sci.* **44**, 2425–2430 (1997).

[24]A. Sitek, G. Gullberg, E. Di Bella, and A. Celler, *J. Nucl. Med.* **42**, 1704–1712 (2001).

[25]T. Farncombe, A. Celler, D. Noll, J. Maeght, and R. Harrop, *IEEE Trans. Nucl. Sci.* **46**, 1055–1061 (1999), ISSN 0018-9499.

[26]A. Celler, T. Farncombe, C. Bever, D. Noll, J. Maeght, R. Harrop, and D. Lyster, *Phys. Med. Biol.* **45**, 3525–3543 (2000).

[27]T. Farncombe, A. Celler, C. Bever, D. Noll, J. Maeght, and R. Harrop, *IEEE Trans. Nucl. Sci.* **48**, 3–9 (2001), ISSN 0018-9499.

[28]T. Farncombe, S. Blinder, A. Celler, D. Noll, J. Maeght, and R. Harrop, "A dynamic expectation maximization algorithm for single camera rotation dynamic SPECT (dSPECT)," in *Nuclear Science Symposium Conference Record, 2000 IEEE*, 2000, pp. 15/31–15/35 vol.2.

[29]L. Shepp, and Y. Vardi, *IEEE Trans. Med. Imag.* **MI-2**, 113–122 (1982).

[30]T. Farncombe, *Functional dynamic SPECT imaging using a single slow camera rotation*, Ph.D. thesis, University of British Columbia, Vancouver, Canada (2000).

[31]J. Qranfal, and G. Tanoh, *Journal of Physics: Conference Series* **124**, 012042 (14pp) (2008), URL `http://stacks.iop.org/1742-6596/124/012042`.

[32]A. Taylor, and J. Ziffer, *Principles and Practices of Nuclear Medicine*, Mosby – Year Book, Inc., 1995, chap. 23: Urinary Tract, 2 edn.

[33]A. Saad, T. Möller, and G. Hamarneh, "PropExplorer: Uncertainty-guided Exploration and Editing of Probabilistic Medical Image Segmentation," in *Computer Graphics Forum (Proceedings of Eurographics/IEEE-VGTC Symposium on Visualization 2010 (EuroVis 2010))*, 2010, vol. 29, pp. 1113–1120.